Fully Compensated Ferrimagnetism with High Magnetic Transition Temperature in a Stable Two-Dimensional Unconventional Stoichiometric CrI Crystal

Siyan Gao(高思妍)[1], Yifeng Zheng(郑益峰)[2], Shuqiang He(何述强)[3], Haiping Fang(方海平)[3*], and Yueyu Zhang(张越宇)[2*]

[1]*School of Materials Science and Engineering, East China University of Science and Technology, Shanghai 200237, China*
[2]*Wenzhou Institute, University of Chinese Academy of Sciences, Wenzhou 325001, China*
[3]*School of Physics, East China University of Science and Technology, Shanghai 200237, China*

(Received 17 January 2025; accepted manuscript online 16 May 2025)

Two-dimensional (2D) fully compensated collinear magnetic materials offer significant advantages for spintronic applications, including robustness against magnetic field perturbations, no stray fields, and ultrafast dynamics. Among these materials, fully compensated ferrimagnets are particularly promising due to their unique characteristics such as the magneto-optical effect, completely spin-polarized currents, and the anomalous Hall effect. We performed a structural search on 2D unconventional stoichiometric Cr–I crystals using a global optimization algorithm. The most stable CrI-$P21/m$ monolayer is a fully compensated ferrimagnetic semiconductor with a band gap of 1.57 eV and a high magnetic transition temperature of 592 K. The spontaneous spin splitting in CrI-$P21/m$ originates from the inequivalent local coordination environments of Cr^1 and Cr^2 ions, yielding a mismatch in their 3d orbitals splitting. Notably, carrier doping at a concentration of 0.01 electrons or holes per atom enables reversible spin polarization, generating a fully spin-polarized current in CrI-$P21/m$. This performance makes it a highly promising candidate for spintronic devices. Our findings not only provide a structural paradigm for discovering fully compensated ferrimagnets but also open a new avenue for designing zero-moment magnetic materials with intrinsic spin splitting.

DOI: 10.1088/0256-307X/42/7/070701 CSTR: 32039.14.0256-307X.42.7.070701

1. Introduction. Fully compensated collinear magnetic materials, a class of collinear magnets with zero magnetic moment, offer exceptional advantages in spintronics, including robustness against external magnetic perturbations, no stray fields, and ultrafast dynamics.[1–6] Conventional collinear antiferromagnets exhibit zero macroscopic magnetization and spin-degenerate features, yet their internal magnetic orders remain challenging to manipulate and detect.[1,2] Spin splitting in band structures is crucial for the practical application of magnets in spintronics.[7,8] The concept of "spin-split" antiferromagnets was first introduced by Pekar and Rashba in 1964.[9] These materials combine zero net magnetization with spin-split characteristics, enabling intriguing phenomena absent in conventional antiferromagnets, such as spin-polarized currents,[10] the anomalous Hall effect,[4] the giant magnetoresistance effect,[11,12] and the Josephson effect.[13] Yuan *et al.* later classified such systems using magnetic symmetry, designating them as the fourth spin splitting prototype (SST-4).[14,15] Subsequently, Šmejkal *et al.* systematically analyzed the symmetry of the "spin-split" collinear antiferromagnets and introduced the term altermagnets.[4,16,17] Altermagnets exhibit spontaneous non-relativistic spin splitting while maintaining compensated magnetic sublattices in real space that are connected by rotational symmetry, which is associated with Fermi-liquid instabilities.[18] Experimental confirmation of altermagnetism was achieved by Krempaský *et al.* in a three-dimensional (3D) MnTe crystal,[19] sparking widespread interest in fully compensated collinear magnetic materials.[20–22] General schemes, such as applying electric fields,[23] stacking engineering,[24] and twisting engineering,[25] have since been employed to generate and manipulate altermagnetism in two-dimensional (2D) van der Waals magnets. Ma *et al.*[26] and Zhu *et al.*[27] demonstrated spin-valley locking and multipiezo effects (e.g., piezoelectricity, piezomagnetism, and piezovalley) in altermagnetic materials.

Fully compensated ferrimagnets constitute a unique class of zero-moment collinear magnets with zero net moment. Unlike conventional ferrimagnets, these materials exhibit vanishing net magnetization while retaining non-relativistic spin splitting along with the absence of symmetry operations connecting their magnetic sublattices, a hallmark property that distinguishes them from antiferromagnets. The concept of fully compensated ferrimagnet was first theoretically predicted by van Leuken and de Groot in 3D Heusler compounds.[28] Since then, research efforts have primarily focused on exploring fully compensated ferrimagnetism in 3D systems.[5,29,30] 2D magnetic

*Corresponding authors. Email: fanghaiping@sinap.ac.cn; zhangyy@wiucas.ac.cn
© 2025 Chinese Physical Society and IOP Publishing Ltd. All rights, including for text and data mining, AI training, and similar technologies, are reserved.

materials[31–34] have garnered significant interest following the experimental observation of intrinsic magnetism in atomically thin CrI_3[35] and $Cr_2Ge_2Te_6$[36] monolayers. Inspired by these developments, Liu *et al.* proposed several feasible approaches to realize fully compensated ferrimagnetism in 2D materials.[37] Two fundamental conditions must be satisfied: (1) the electron occupancy in orbitals with opposite spin channels must be equal, and (2) there must be no symmetry operation connecting the magnetic sublattices.

The ground state electron configuration of Cr atoms is $[Ar]3d^54s^1$. In Cr-based compounds where a Cr atom donates one electron to a halogen (e.g., iodine), the resulting Cr ion adopts a $3d^5$ valence configuration. The half-filled 3d orbitals of the Cr ion provide a unique platform for electron hopping between orbitals with opposite spins, which is crucial for realizing fully compensated ferrimagnetism. In this work, we employed a global optimization algorithm to predict a series of stable 2D Cr–I crystals with an unconventional stoichiometric ratio[38,39] of 1:1. Spin-polarized first-principles calculations revealed that the CrI-$P21/m$ monolayer (spin space group:[40,41] $P^12_1/^1m^{\infty m}1$) is a fully compensated ferrimagnetic semiconductor with a band gap of 1.57 eV. In contrast, the CrI-$P\bar{3}m1$, CrI-*Pbcm*, and CrI-*Abm*2 monolayers are antiferromagnetic (AFM) semiconductors, featuring larger band gaps ranging from 2.40 eV to 2.80 eV. We uncovered the origin of the distinct electronic structures in these CrI monolayers and elucidated the physical mechanism underlying the spontaneous spin splitting in the CrI-$P21/m$ monolayer. Additionally, Monte Carlo simulations were performed to estimate their magnetic transition temperatures. Finally, we evaluated the potential of the CrI-$P21/m$ monolayer for spintronic applications by systematically analyzing its electronic structure under both electron and hole doping.

2. Computational Methods. A structural search of 2D Cr–I crystals composed of chromium (Cr) and iodine (I) with an atomic ratio of 1:1 was performed using the global optimization algorithm, as implemented in the inverse design of materials by multi-objective differential evolution (IM^2ODE) package.[42] A series of crystal structures of CrI monolayers were obtained based on the differential evolution (DE) algorithm,[43] with the total energy serving as the target function. During the process, 30 DE iteration steps and 30 populations for each DE step were chosen. In each DE step, 30 initial structures were generated, followed by ranking, selecting, and creating new structures. In each DE step, 60% of the crystal structures were inherited from the previous iteration while 40% of the crystal structures were randomly created. The crystal structures generated in each DE step were fully relaxed using the Vienna *ab initio* simulation package (VASP).[44]

Spin-polarized density functional theory (DFT) calculations were performed using the VASP.[44] The projector-augmented wave method[45,46] was employed to describe electron–ion interaction, with the Perdew–Burke–Ernzerhof (PBE) functional[47] of the generalized gradient approximation used for exchange-correlation interaction. An energy cutoff of 500 eV was chosen to expand the plane wave basis. Structural relaxations were conducted until the convergence criteria of 10^{-8} eV for total energy and 10^{-4} eV/Å for Hellmann–Feynman forces were met. The atomic positions and lattice parameters were fully optimized. A 20 Å vacuum spacing was introduced to eliminate the interactions between periodic replicas. Brillouin zone was sampled using the Monkhorst pack scheme[48] with grids of $24 \times 14 \times 1$ for a unit cell of the CrI-$P21/m$ monolayer, $24 \times 24 \times 1$ for a unit cell of the CrI-$P\bar{3}m1$ monolayer, $14 \times 21 \times 1$ for a unit cell of the CrI-*Pbcm* monolayer, and $24 \times 14 \times 1$ for a unit cell of the CrI-*Abm*2 monolayer, respectively. The DFT+U correction with an effective U value of 3 eV was considered for Cr 3d states. Phonon calculations were performed using the finite-displacement supercell approach in the PHONOPY code,[49] with consideration of higher-order phonon modes via the hiPhive python package.[50,51] A $5 \times 3 \times 1$ supercell of CrI-$P21/m$ monolayer with a $5 \times 5 \times 1$ k-mesh, a $4 \times 4 \times 1$ supercell of CrI-$P\bar{3}m1$ monolayer with a $6 \times 6 \times 1$ k-mesh, a $3 \times 4 \times 1$ supercell of CrI-*Pbcm* monolayer with a $5 \times 5 \times 1$ k-mesh, and a $4 \times 2 \times 1$ supercell of CrI-*Abm*2 monolayer with a $4 \times 5 \times 1$ k-mesh were adopted in the phonon calculations. Population analysis was performed on the predicted CrI monolayers using the Bader charge analysis code, which was developed by Henkelman's group.[52,53] An *ab initio* molecular dynamics (AIMD) simulation was performed on a $5 \times 3 \times 1$ supercell of the CrI-$P21/m$ monolayer (size: 20.67 Å × 21.47 Å × 26.00 Å) using the NVT canonical ensemble with the Nosé–Hoover thermostat at 300 K, as implemented in the VASP package.[44] The simulation was allowed to run for 4.8 ps with a time step of 1 fs. Monte Carlo simulations[54–56] employing the Metropolis algorithm were performed on $32 \times 32 \times 1$ supercells to determine the magnetic transition temperature of the predicted CrI monolayers, as implemented in the open source MCSOLVER package.[57] At each temperature, the system was equilibrated through 80,000 sweeps, followed by an additional 800,000 sweeps from which all thermodynamic averages were obtained.

3. Results and Discussion. To search 2D fully compensated collinear magnetic materials exhibiting high magnetic transition temperatures, we performed a global optimization search of 2D Cr–I binary compounds using the IM^2ODE package.[42] Focusing on unexplored Cr–I crystals with an unconventional stoichiometric ratio of 1:1, we discovered eight different CrI monolayers characterized by their space groups: CrI-$P21/m$, CrI-$P\bar{3}m1$, CrI-*Pbcm*, CrI-*Abm*2, CrI-$P4/nmm$, CrI-*Pbam*, CrI-$P\bar{6}m2$, and CrI-$P4/mmm$. The structural phase diagram was constructed through comparing their total energies [Fig. 1(a) and Table S1 of Supplymentary Materials (SM)]. The total energies of these CrI monolayers follow the order of CrI-$P21/m$ < CrI-$P\bar{3}m1$ < CrI-*Pbcm* < CrI-*Abm*2 < CrI-$P4/nmm$ < CrI-*Pbam* < CrI-$P\bar{6}m2$ < CrI-$P4/mmm$. Table 1 summarizes the lattice parameters of the predicted CrI monolayers.

Table 1. Lattice parameters and formation energies of the CrI-$P21/m$, CrI-$P\bar{3}m1$, CrI-$Pbcm$, and CrI-$Abm2$ monolayers.

Material	a (Å)	b (Å)	c (Å)	α (deg)	β (deg)	γ (deg)	E_f (eV/atom)
$P21/m$	4.13	7.16	26.00	90	90	90	−0.42
$P\bar{3}m1$	4.55	4.55	24.00	90	90	120	−0.30
$Pbcm$	7.13	4.86	23.95	90	90	90	−0.30
$Abm2$	4.97	7.36	23.77	90	90	90	−0.29

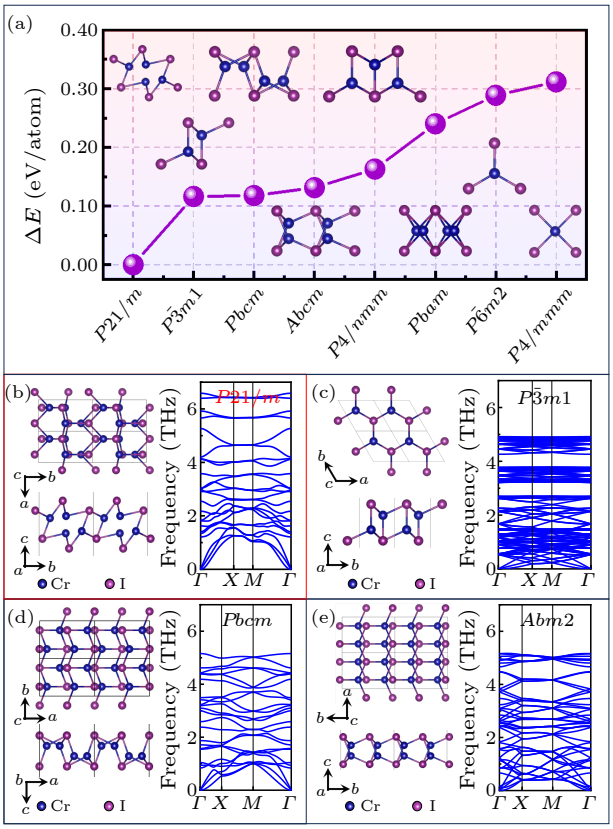

Fig. 1. (a) Structural phase diagram of CrI monolayers obtained from the global optimization search at a first-principles level. The total energy of the most stable phase (CrI-$P21/m$) is set to zero. Insets: Side views of the predicted CrI monolayers with different space groups. Crystal structures (top and side views) and phonon spectra of the four lowest-energy phases in (b) CrI-$P21/m$, (c) CrI-$P\bar{3}m1$, (d) CrI-$Pbcm$, and (e) CrI-$Abm2$. The navy blue and purple spheres represent the Cr and I ions, respectively. The unit cell is marked by black lines.

Since the stability is crucial for the experimental synthesis of theoretically predicted materials, we investigated the energetical, thermodynamic, dynamic, and thermal stabilities of the predicted CrI monolayers. The formation energy E_f of the Cr–I crystals is defined as

$$E_f = [E(\text{Cr–I}) - mE(\text{Cr}) - nE(\text{I})]/(m+n), \quad (1)$$

where E(Cr–I) is the total energy of the Cr–I crystals per unit cell; E(Cr) and E(I) are the total energies in the bulk Cr crystal and I_2 molecular crystal per atom, respectively; m and n are the numbers of Cr and I atoms contained in a unit cell of the Cr–I crystals, respectively. The negative values of formation energies reveal that all CrI monolayers are energetically stable (Table 1 and Table S2 of SM). In particular, the CrI-$P21/m$ monolayer has the lowest formation energy of −0.42 eV/atom.

To assess the thermodynamic stability of CrI monolayers, we constructed a convex hull diagram of the formation energy for Cr–I crystals (Fig. S1 of SM). The hull was constructed using experimentally synthesized stable binary Cr–I compounds (CrI_3 crystals) and the pure elemental bulk crystals (Cr and I_2 crystals), all of which are available on the Materials Project database.[58] All lattice parameters and atomic positions were fully relaxed. The formation energy E_f of the Cr–I crystals was calculated using Eq. (1). The most stable CrI-$P21/m$ monolayer lies 37.51 meV/atom above the convex hull line (Fig. S1 of SM), which indicates that these CrI monolayers are metastable phases. As expected, bulk CrI_3 crystal emerges as the most thermodynamically stable phase among all Cr–I crystals. We note that metastable phases with formation energies slightly above the hull are experimentally accessible, as demonstrated in prior studies.[59–61]

Figures 1(b)–1(e) and Fig. S2 of SM show the phonon spectra of the predicted CrI monolayers. There is no negative imaginary frequency in the phonon spectra of the CrI-$P21/m$, CrI-$P\bar{3}m1$, CrI-$Pbcm$, and CrI-$Abm2$ monolayers [Figs. 1(b)–1(e)], which indicates that these CrI monolayers are dynamically stable. By contrast, the CrI-$P4/nmm$, CrI-$Pbam$, CrI-$P\bar{6}m2$, and CrI-$P4/mmm$ monolayers exhibit a large negative imaginary frequency (Fig. S2 of SM), indicating that they are dynamically unstable.

To confirm the thermal stability of the CrI-$P21/m$ monolayer, we performed the AIMD simulation at 300 K for 7.7 ps. As shown in Fig. S3 of SM, the temperature converges well over time, and the free energy shows an increasing trend at the beginning and then converges well over time. The CrI-$P21/m$ remains stable during the AIMD simulation at 300 K, with no bond breaking (Fig. S4 of SM). This indicates that the CrI-$P21/m$ monolayer is thermally stable at 300 K. Based on these results, we selected the CrI-$P21/m$, CrI-$P\bar{3}m1$, CrI-$Pbcm$, and CrI-$Abm2$ monolayers for further investigation.

The preferred magnetic structure of four stable CrI monolayers was determined by comparing the total energies of different magnetic configurations: one ferromagnetic and five AFM configurations. We employed $4\times4\times1$ supercells for the CrI-$P21/m$ (Fig. S5) and CrI-$P\bar{3}m1$ (Fig. S6) monolayers and $3\times3\times1$ supercells for the CrI-$Pbcm$ (Fig. S7) and CrI-$Abm2$ (Fig. S8) monolayers. Our calculations reveal a strong preference for AFM ordering across all four CrI monolayers (Table S3). The CrI-$P21/m$ monolayer with the AFM1 state exhibits the lowest energy, and the CrI-$Pbcm$ monolayer prefers an AFM3 configuration. Both CrI-$P\bar{3}m1$ and CrI-$Abm2$ monolayers favor an A-type AFM configuration with intralayer ferromagnetism and interlayer antiferromagnetism.

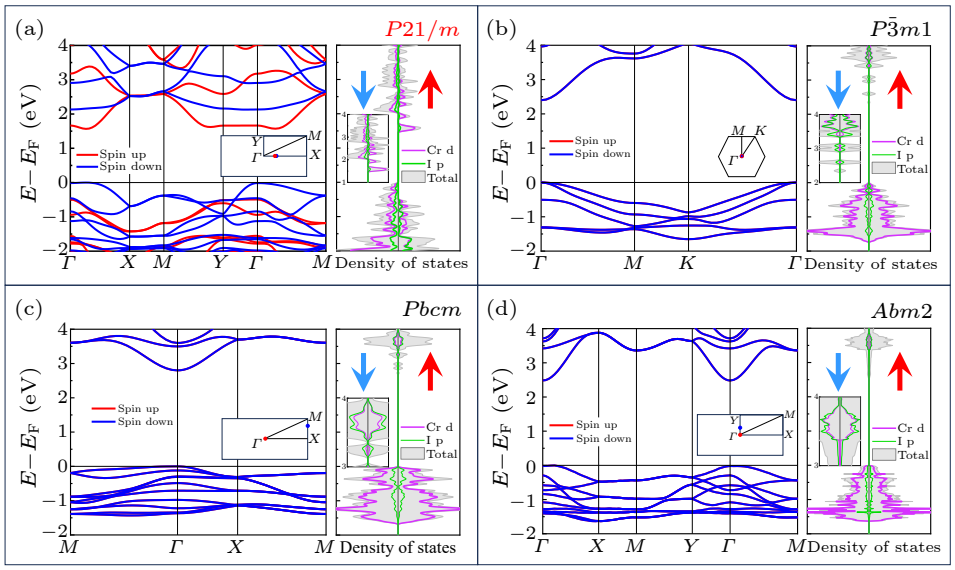

Fig. 2. Spin-polarized electronic band structures, total density of states, and projected density of states of the (a) CrI-$P21/m$, (b) CrI-$P\bar{3}m1$, (c) CrI-*Pbcm*, and (d) CrI-*Abm*2 monolayers using the HSE06 functional. Left panel insets: Selection of k-point path in the Brillouin zone for each CrI monolayer, with blue and red circles marking the valence band maximum and conduction band minimum, respectively. Right panel insets: Magnified views of the unoccupied states near the Fermi level for each CrI monolayer.

The spin-polarized band structures of the CrI monolayers were calculated using the HSE06 functional to investigate their magnetic properties. Spin splitting is observed in the band structure of the CrI-$P21/m$ monolayer, a semiconductor with a band gap of 1.57 eV [Fig. 2(a)]. In contrast, the CrI-$P\bar{3}m1$, CrI-*Pbcm*, and CrI-*Abm*2 monolayers are AFM semiconductors, exhibiting band gaps of 2.40, 2.80, and 2.49 eV, respectively [Figs. 2(b)–2(d)]. The valence band maximum (VBM) states of the CrI-$P21/m$, CrI-$P\bar{3}m1$, CrI-*Pbcm*, and CrI-*Abm*2 monolayers are dominated by the Cr d orbital and I p orbital [right panels in Figs. 2(a)–2(d)]. The conduction band minimum (CBM) state of the CrI-$P21/m$ monolayer is mainly contributed by the Cr d orbital [right panel in Fig. 2(a)], while the Cr d and I p orbitals contribute to the CBM states of the CrI-$P\bar{3}m1$, CrI-*Pbcm*, and CrI-*Abm*2 monolayers [right panel in Figs. 2(b)–2(d)]. Partial charge density of the CBM and VBM states of the CrI monolayers further confirms the above results. For the CrI-$P21/m$ monolayer, the CBM state is attributed to the d orbitals of the Cr ions, while both the d orbitals of the Cr ions and the p orbitals of the I ions contribute to the VBM state (Fig. S9). For the CrI-$P\bar{3}m1$ (Fig. S10), CrI-*Pbcm* (Fig. S11), and CrI-*Abm*2 (Fig. S12) monolayers, both the CBM and VBM states are contributed by the d orbitals of the Cr ions and the p orbitals of the I ions.

The four stable CrI monolayers exhibit distinct electronic structures, primarily characterized by the presence or absence of spin splitting in their band structures. Given the pivotal role of Cr 3d orbitals in governing the magnetic properties of these materials, it is necessary to analyze the local chemical environments of Cr ions across all four phases to elucidate the physical origin of spin splitting in the CrI-$P21/m$ monolayer. The unit cell of the CrI-$P21/m$ monolayer contains four Cr and four I ions. Unlike other CrI monolayers (CrI-$P\bar{3}m1$, CrI-*Pbcm*, and CrI-*Abm*2) that contain only one type of Cr and I ion, the CrI-$P21/m$ monolayer features two types of each element, as evidenced by their Wyckoff positions in Table S4. The CrI-$P21/m$ monolayer exhibits two distinct local coordination environments for both Cr and I ions. One type of the Cr ion (hereafter referred to as Cr^1) is bonded to four I ions, while another type of the Cr ion (hereafter referred to as Cr^2) is bonded to three I ions [Figs. 3(c) and 3(d)]. A comparable scenario is observed in the case of the I ions: One type of the I ion (hereafter referred to as I^1) is bonded to four Cr ions, while another type of the I ion (hereafter referred to as I^2) is bonded to three Cr ions [Fig. S13]. Bader charge analysis was performed to evaluate the charge transfer in the CrI-$P21/m$ monolayer. Each Cr^1 and Cr^2 atom loses 0.60 and 0.50 electrons, respectively, while each I^1 and I^2 atom gains 0.58 and 0.52 electrons, respectively (Table S5). The differential charge transfer between the Cr^1 and Cr^2 atoms and between the I^1 and I^2 atoms further confirms their inequivalent local chemical environments. The spin charge density [Fig. 3(b)] of the CrI-$P21/m$ monolayer reveals that Cr^2 ions dominate the spin-up channel, and Cr^1 ions primarily contribute to the spin-down channel. Notably, the spin-up and spin-down charge densities exhibit distinct spatial distributions, contrasting sharply with the symmetric patterns observed in CrI-$P\bar{3}m1$, CrI-*Pbcm*, and CrI-*Abm*2 monolayers (Fig. S14).

In CrI monolayers, the Cr 4s orbital donates one electron to the I 5p orbital, forming an ionic bond between Cr and I atoms. The remaining five electrons half-occupy Cr 3d orbitals, giving rise to a magnetic moment of 5 μB. This aligns with spin-polarized DFT results (∼4.05 μB and ∼3.99 μB for each Cr^1 and Cr^2 ion in the CrI-$P21/m$;

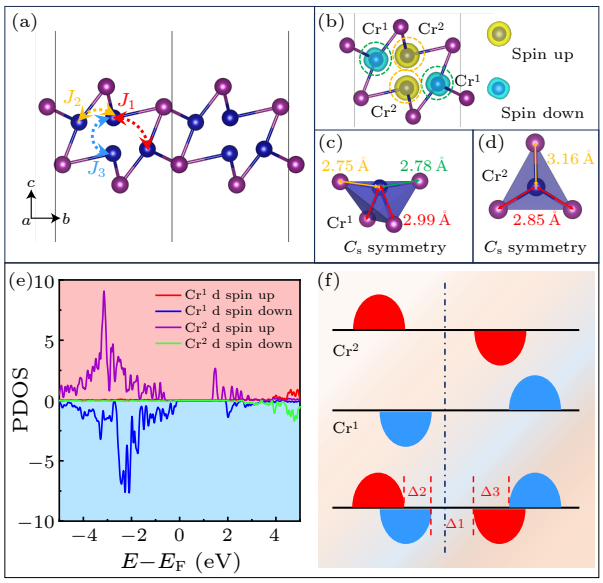

Fig. 3. (a) Exchange paths between the nearest-neighbor, next-nearest-neighbor, and third-nearest-neighbor Cr ions in the CrI-$P21/m$ monolayer. (b) Spin charge density of the CrI-$P21/m$ monolayer with an isosurface of 0.06e/bohr^3 for both spin directions. The yellow and blue areas denote the spin-up and spin-down channels, respectively. Local coordination environments of the (c) Cr^1 and (d) Cr^2 ions in the CrI-$P21/m$ monolayer. (e) Partial density of states (PDOS) of the CrI-$P21/m$ monolayer with respect to the d orbitals of Cr^1 and Cr^2 ions. (f) Schematic illustration of the staggered energy level in Cr^1 and Cr^2 ions.

∼4.24 μB for each Cr ion in the CrI-$P\bar{3}m1$; ∼4.20 μB for each Cr ion in the CrI-*Pbcm*; ∼4.22 μB for each Cr ion in the CrI-*Abm*2). Both Cr^1 and Cr^2 ions of CrI-$P21/m$ reside in Cs-symmetric coordination fields, splitting their 3d orbitals of Cr^1 and Cr^2 ions into A′($d_{x^2-y^2}$), A′(d_{xy}), A′(d_{z^2}), A″(d_{xz}), and A″(d_{yz}). We calculated the local density of states of the CrI-$P21/m$ monolayer with respect to the Cr^1 and Cr^2 ions [Fig. 3(e)]. The Cr^1 ion predominantly contributes to the energy levels in the spin-down channel, and the Cr^2 ion is primarily responsible for the energy levels in the spin-up channel. We further calculated the d band centers ε_d for the occupied orbitals $d_{x^2-y^2}$, d_{xy}, d_{z^2}, d_{xz}, and d_{yz} of both Cr^1 and Cr^2 ions (Fig. S15). Apparently, a staggered alignment of ε_d of the Cr^1 and Cr^2 ions originates from their inequivalent local coordination environments, leading to the spin-splitting mismatch of 3d orbitals of Cr^1 and Cr^2 ions.

In the CrI-$P\bar{3}m1$ monolayer, the 3d orbitals of Cr ions split into one single degenerate $A_1(d_{z^2})$, two double degenerate E($d_{x^2-y^2}$, d_{xy}) and E(d_{xz}, d_{yz}) according to the C_{3v} symmetric crystal field of the Cr ion [Fig. S16(a)]. For the CrI-*Pbcm* and CrI-*Abm*2 monolayers, the 3d orbitals of Cr ions split into A′($d_{x^2-y^2}$), A′(d_{xy}), A′(d_{z^2}), A″(d_{xz}), and A″(d_{yz}) in the C_s-symmetric crystal field [Figs. S16(b) and S16(c)]. The equivalent local coordination environments of the Cr ions in the CrI-$P\bar{3}m1$, CrI-*Pbcm*, and CrI-*Abm*2 monolayers result in the identical spin splitting of 3d orbitals of the Cr ions.

Symmetry plays a significant role in understanding spin-splitting behavior in magnetic materials. When the non-relativistic effect is considered in the predicted CrI monolayers, the spin space and real space are decoupled. We described the CrI monolayers by the spin space group using the FINDSPINGROUP online program developed by Liu's group.[40,41] Table S7 summarizes the spin space groups and symmetry operations of the CrI-$P21/m$, CrI-$P\bar{3}m1$, CrI-*Pbcm*, and CrI-*Abm*2 monolayers. The CrI-$P21/m$ is identified by the spin space group of $P^12_1/^1m^{\infty m}1$. The CrI-$P21/m$ is a compensated ferrimagnet because two conditions are fulfilled: there are no symmetry operators connecting two sublattices in the CrI-$P21/m$ (Table S7), and the $3d^5$ electron configuration of Cr ions results in equal occupation of spin-up and spin-down channels. The CrI-*Abm*2 monolayer is described by the spin space group of $A^{-1}e^1m^{-1}2^{\infty m}1$, which belongs to the symmetry of altermagnets. However, no spin splitting is observed in its band structure. This can be explained by the work of He *et al.*,[62] who demonstrated that 2D materials impose stricter symmetry requirements for spin splitting compared to their 3D counterparts. Specifically, the presence of in-plane PT symmetry, indicated by the symmetry operator $\{-1||2_{001}\}$, forbids the spin splitting in the band structure of the CrI-*Abm*2 monolayer (Table S6). The CrI-$P\bar{3}m1$ and CrI-*Pbcm* monolayers are conventional antiferromagnets with spin space groups of $P^{-1}\bar{3}^1m^11^{\infty m}1$ and $P^1b^{-1}c^1m^{\infty m}1$, respectively, both of which contain PT symmetry (Table S7).

To further determine the detailed magnetic structures, we employed the Heisenberg model to construct the spin Hamiltonian of the CrI monolayers,

$$H_{\text{spin}} = -\sum_{ij} J_{ij}\boldsymbol{S}_i \cdot \boldsymbol{S}_j + A\sum_i (S_i)^2, \qquad (2)$$

where $\boldsymbol{S}_i$ denotes the spin vector at the ith site, J_{ij} is the parameter of the exchange interaction between the magnetic Cr ions at the ith and jth sites, and A is the parameter of single-ion magnetic anisotropy. For CrI-$P21/m$ [Fig. 3(a)] and CrI-*Pbcm* (Fig. S17), we considered three exchange interactions (J_1, J_2, and J_3) between the nearest-neighbor, next-nearest-neighbor, and third-nearest-neighbor Cr ions. For CrI-$P\bar{3}m1$ and CrI-*Abm*2, only two exchange interactions (J_1 and J_2) between the nearest-neighbor and next-nearest-neighbor Cr ions were included (Fig. S17). We calculated the magnetic parameters of the exchange interactions based on the four-states method.[63] The negative values of magnetic parameters represent the AFM exchange interactions between the Cr ions (Table 2). The AFM exchange interactions arise from half-filled 3d orbitals of the Cr ions, where electron hopping is permitted only between the occupied and empty orbitals with opposite spin arrangement.

As the magnetic anisotropy is essential for stabilizing 2D magnetism against thermal fluctuations, we calculated the magnetic anisotropic energy (MAE) of the xz and xy planes in the CrI-$P21/m$, CrI-$P\bar{3}m1$, CrI-*Pbcm*, and CrI-*Abm*2 monolayers (Fig. 4). The CrI-$P21/m$ [Fig. 4(a)], CrI-*Pbcm* [Fig. 4(c)], and CrI-*Abm*2 [Fig. 4(d)] monolayers

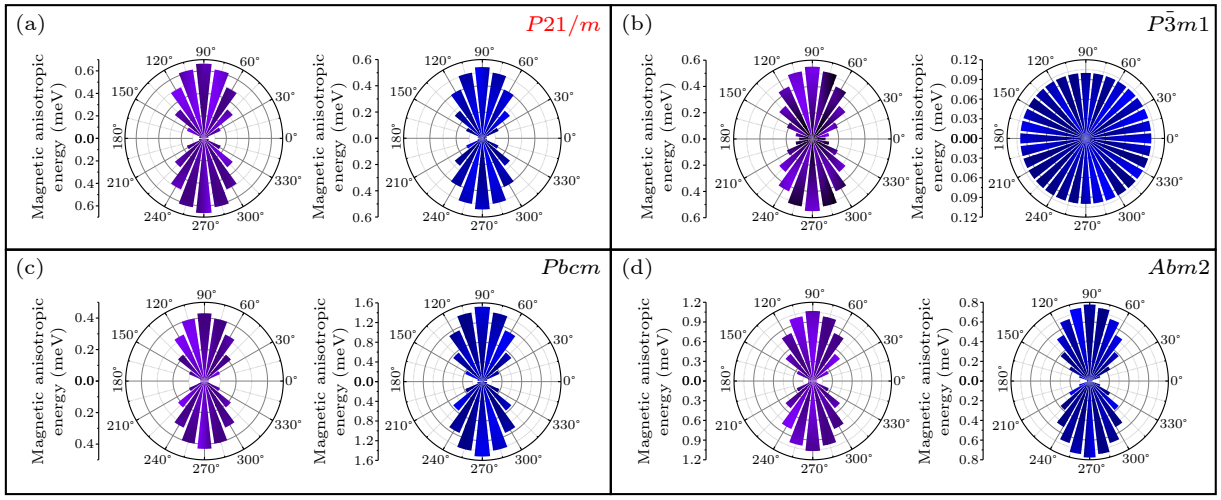

Fig. 4. Magnetic anisotropic energy of the xz plane (left panels) and xy plane (right panels) in the (a) CrI-$P21/m$, (b) CrI-$P\bar{3}m1$, (c) CrI-$Pbcm$, and (d) CrI-$Abm2$ monolayers. For CrI-$P21/m$, CrI-$Pbcm$, and CrI-$Abm2$ monolayers, the energy of the easy axis is set to 0 meV. For CrI-$P\bar{3}m1$, the energy of the easy plane is set to 0.1 meV to highlight its in-plane anisotropy. The x axis is set to 0°.

Table 2. The magnetic parameters (J_1, J_2, and J_3) of the exchange interactions between the nearest-neighbor, next-nearest-neighbor, and third-nearest-neighbor Cr ions, the parameter of single-ion anisotropy energy A, and magnetic transition temperature T in the CrI-$P21/m$, CrI-$P\bar{3}m1$, CrI-$Pbcm$, and CrI-$Abm2$ monolayers.

Material	J_1 (meV)	J_2 (meV)	J_3 (meV)	A (meV)	T (K)
$P21/m$	−153.54	−137.29	−59.43	−0.17	592
$P\bar{3}m1$	−73.08	−8.71	–	−0.23	201
$Pbcm$	−81.44	−56.79	−23.64	−0.38	380
$Abm2$	−95.06	−15.55	–	−0.27	324

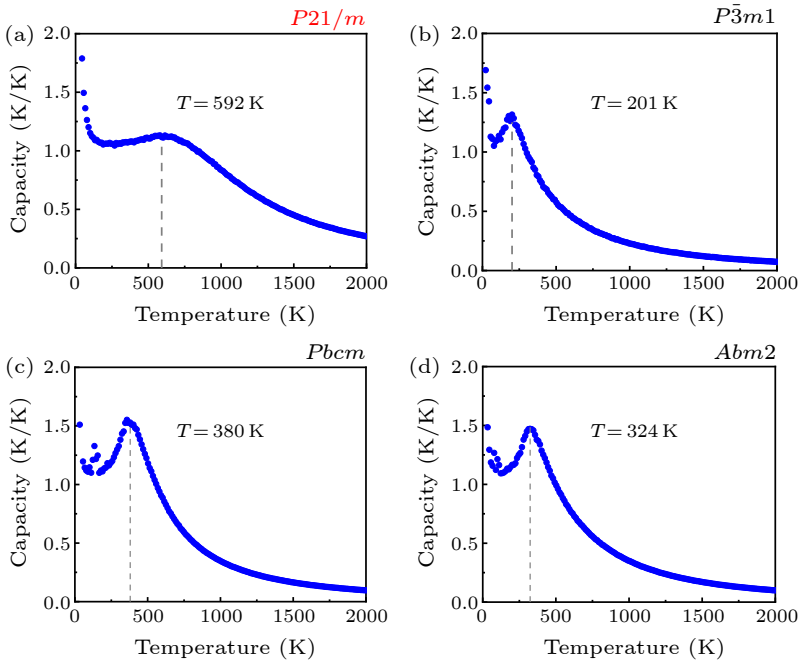

Fig. 5. Evolution of the specific heat capacity per Cr ion over temperature in the (a) CrI-$P21/m$, (b) CrI-$P\bar{3}m1$, (c) CrI-$Pbcm$, and (d) CrI-$Abm2$ monolayers.

have an easy axis along the x axis, while the CrI-$P\bar{3}m1$ monolayer has an easy plane of the xy plane [Fig. 4(b)]. The calculated MAE of the CrI-$P21/m$, CrI-$P\bar{3}m1$, CrI-$Pbcm$, and CrI-$Abm2$ monolayers is 0.17, 0.23, 0.38, and 0.27 meV/atom, respectively.

We performed Monte Carlo simulations based on the Heisenberg model with on-site MAE (Table 2) to estimate the magnetic transition temperatures of the CrI-$P21/m$, CrI-$P\bar{3}m1$, CrI-$Pbcm$, and CrI-$Abm2$ monolayers. Figure 5 shows the evolution of the specific heat

capacity per Cr ion over temperature in the CrI-$P21/m$, CrI-$P\bar{3}m1$, CrI-$Pbcm$, and CrI-$Abm2$ monolayers. For the CrI-$P21/m$ monolayer, the specific heat capacity peaks at around 592 K [Fig. 5(a)], significantly above room temperature. This high magnetic transition temperature is attributed to its geometric structure. The distances between the nearest-neighbor, next-nearest-neighbor, and third-nearest-neighbor Cr ions are 2.82, 2.97, and 3.00 Å, respectively. The short distances between these Cr ions allow for a large overlap of d orbitals of three Cr ion pairs, resulting in a strong AFM direct exchange interaction in the CrI-$P21/m$ monolayer. For the CrI-$P\bar{3}m1$ monolayer, the competing AFM interactions between the nearest-neighbor and next-nearest-neighbor Cr ions, as well as the honeycomb spin lattice stacked from two triangular layers, would typically induce magnetic frustration. However, the incorporation of on-site MAE stabilizes the AFM order, leading to a phase transition point at 201 K [Fig. 5(b)]. Additionally, a peak at around 380 K is found in the specific heat capacity curves of the CrI-$Pbcm$ monolayer [Fig. 5(c)], and the CrI-$Abm2$ monolayer exhibits a peak of specific heat capacity at 324 K [Fig. 5(d)].

Since the band structure of CrI-$P21/m$ monolayer is similar to that of the bipolar antiferromagnetic semiconductor, we described it with three energy gap parameters, including Δ_1, Δ_2, and Δ_3 [Fig. 3(f)]. In general, the spin-flip gap Δ_1 should be small enough to allow for the shift of the Fermi level into either the spin-up or spin-down channel via the gate voltage or carrier doping, and Δ_2 and Δ_3 should be large enough to ensure the stability of a half-metallic gap during the modulation. Here, the values of Δ_1, Δ_2, and Δ_3 for the CrI-$P21/m$ monolayer are 1.57 eV, 0.49 eV, and 0.56 eV, respectively, which satisfies the above requirements.

To evaluate the potential of the CrI-$P21/m$ monolayer for spintronic applications, we modulated its electronic structure via electron or hole doping at carrier concentrations ranging from 0.01 to 0.04 electrons or holes per atom (Fig. S18). Figure 5 shows the spin-polarized band structures of the CrI-$P21/m$ monolayer, calculated using the PBE functional, under electron or hole doping at carrier concentrations of 0.01 and 0.04 electrons or holes per atom. Under electron doping, the Fermi level shifts into the CBM region, generating a fully spin-up-polarized current. By contrast, hole doping induces the Fermi level shift into the VBM region, producing a fully spin-down-polarized current. This result indicates that the CrI-$P21/m$ monolayer can be shifted from a fully compensated ferrimagnetic semiconductor to a fully compensated ferrimagnetic half-metal by applying low-density electron or hole doping, demonstrating exceptional promise for next-generation spintronic applications.

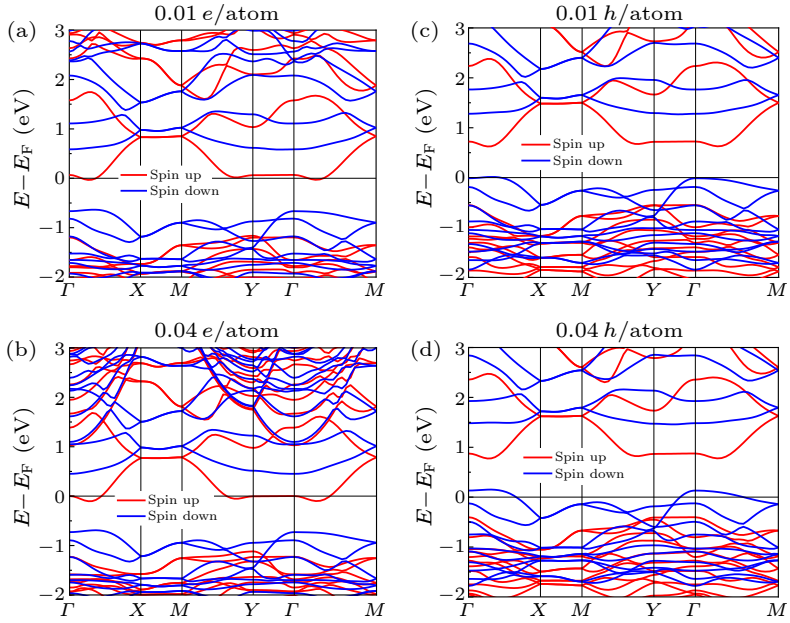

Fig. 6. Band structures of the CrI-$P21/m$ monolayer for (a) and (b) electron doping with a carrier concentration of 0.01 and 0.04 electrons per atom; (c) and (d) hole doping with a carrier concentration of 0.01 and 0.04 holes per atom.

4. Conclusions. In conclusion, we predicted a series of stable CrI monolayers with unconventional stoichiometric ratios, including CrI-$P21/m$, CrI-$P\bar{3}m1$, CrI-$Pbcm$, and CrI-$Abm2$ monolayers, aiming to discover novel 2D zero-moment magnetic materials capable of generating fully spin-polarized currents, such as fully compensated ferrimagnets. Among these, the CrI-$P21/m$ monolayer has been identified as a fully compensated ferrimagnetic semiconductor with a band gap of 1.57 eV. The spontaneous spin-splitting nature of CrI-$P21/m$ originates from the inequivalent local coordination environment of Cr^1 and Cr^2 ions, resulting in the mismatch of 3d orbitals of Cr^1 and Cr^2 ions. Remarkably, the CrI-$P21/m$ monolayer exhibits a high magnetic transition temperature of 592 K, making it particularly suitable for practical spintronic applications. Through carrier doping at a concentration as low as 0.01 electron or hole per atom, the CrI-$P21/m$ monolayer can be precisely modulated to generate a completely spin-

polarized current. Additionally, the CrI-$P\bar{3}m1$, CrI-$Pbcm$, and CrI-$Abm2$ monolayers of AFM semiconductors are also expected to exhibit fantastic physical properties. We believe that the CrI-$P21/m$ monolayer predicted in this work holds great potential for practical spintronic applications, and the discovery of the CrI-$P21/m$ monolayer provides a structural paradigm and a design idea for searching for novel fully compensated ferrimagnets.

Acknowledgements. This work was supported by the Natural Science Foundation of Wenzhou Institute, University of Chinese Academy of Sciences (UCAS) (Grant No. WIUCASQD2023004), the National Natural Science Foundation of China (Grant Nos. 12304006, 12404265, and 12435001), the Natural Science Foundation of Shanghai, China (Grant No. 23JC1401400), the Natural Science Foundation of Wenzhou (Grant No. L2023005), and the Fundamental Research Funds for the Central Universities of East China University of Science and Technology. The computational resources are provided by the High-Performance Computing Cluster of Wenzhou Institute, UCAS, and Inner Mongolia Zhongke Supercomputing Technology Co., Ltd.

References

[1] Jungwirth T, Marti X, Wadley P, and Wunderlich J 2016 *Nat. Nanotechnol.* **11** 231
[2] Baltz V, Manchon A, Tsoi M, Moriyama T, Ono T, and Tserkovnyak Y 2018 *Rev. Mod. Phys.* **90** 015005
[3] Šmejkal L, Mokrousov Y, Yan B, and MacDonald A H 2018 *Nat. Phys.* **14** 242
[4] Šmejkal L, González-Hernández R, Jungwirth T, and Sinova J 2020 *Sci. Adv.* **6** eaaz8809
[5] Semboshi S, Umetsu R Y, Kawahito Y, and Akai H 2022 *Sci. Rep.* **12** 10687
[6] Zhang Y C, Bai H, Zhang D H, Chen C, Han L, Liang S X, Chu R Y, Dai J K, Sawicki M, Pan F, and Song C 2024 *Chin. Phys. Lett.* **42** 027301
[7] Mazin I I, Koepernik K, Johannes M D, González-Hernández R, and Šmejka L 2021 *Proc. Natl. Acad. Sci. U.S.A* **118** e2108924118
[8] Hayami S, Yanagi Y, and Kusunose H 2019 *J. Phys. Soc. Jpn.* **88** 123702
[9] Pekar S I and Rashba E I 1964 *J. Exptl. Theoret. Phys.* **47** 1927
[10] Naka M, Hayami S, Kusunose H, Yanagi Y, Motome Y, and Seo H 2019 *Nat. Commun.* **10** 4305
[11] Šmejkal L, Hellenes A B, González-Hernández R, Sinova J, and Jungwirth T 2022 *Phys. Rev. X* **12** 011028
[12] Shao D F, Zhang S H, Li M, Eom C B, and Tsymbal E Y 2021 *Nat. Commun.* **12** 7061
[13] Ouassou J A, Brataas A, and Linder J 2023 *Phys. Rev. Lett.* **131** 076003
[14] Yuan L D, Wang Z, Luo J W, Rashba E I, and Zunger A 2020 *Phys. Rev. B* **102** 014422
[15] Yuan L D, Wang Z, Luo J W, and Zunger A 2021 *Phys. Rev. Mater.* **5** 014409
[16] Šmejkal L, Sinova J, and Jungwirth T 2022 *Phys. Rev. X* **12** 031042
[17] Šmejkal L, Sinova J, and Jungwirth T 2022 *Phys. Rev. X* **12** 040501
[18] Wu C, Sun K, Fradkin E, and Zhang S C 2007 *Phys. Rev. B* **75** 115103
[19] Krempasky J, Šmejkal L, D'souza S W, Hajlaoui M, Springholz G, Uhlířová K, Alarab F, Constantinou P C, Strocov V, Usanov D, Pudelko W R, González-Hernández R, Birk Hellenes A, Jansa Z, Reichlová H, Šobáň Z, Gonzalez Betancourt R D, Wadley P, Sinova J, Kriegner D, Minár J, Dil J H, and Jungwirth T 2024 *Nature* **626** 517
[20] Duan X, Zhang J, Zhu Z, Liu Y, Zhang Z, Žutić I, and Zhou T 2025 *Phys. Rev. Lett.* **134** 106801
[21] Jiang B, Hu M, Bai J, Song Z, Mu C, Qu G, Li W, Zhu W, Pi H, Wei Z, Sun Y J, Huang Y, Zheng X, Peng Y, He L, Li S, Luo J, Li Z, Chen G, Li H, Weng H, and Qian T 2025 *Nat. Phys.* **21** 754
[22] Guo S D and Ang Y S 2023 *Phys. Rev. B* **108** L180403
[23] Wang D, Wang H, Liu L, Zhang J, and Zhang H 2024 *Nano Lett.* **25** 498
[24] Zeng S and Zhao Y J 2024 *Phys. Rev. B* **110** 174410
[25] Liu Y, Yu J, and Liu C C 2024 *Phys. Rev. Lett.* **133** 206702
[26] Ma H Y, Hu M, Li N, Liu J, Yao W, Jia J F, and Liu J 2021 *Nat. Commun.* **12** 2846
[27] Zhu Y, Chen T, Li Y, Qiao L, Ma X, Liu C, Hu T, Gao H, and Ren W 2023 *Nano Lett.* **24** 472
[28] Van Leuken H and De Groot R A 1995 *Phys. Rev. Lett.* **74** 1171
[29] Venkateswara Y, Gupta S, Samatham S S, Varma M R, Enamullah, Suresh K G, and Alam A 2018 *Phys. Rev. B* **97** 054407
[30] Galanakis I, Özdoğan K, Şaşıoğlu E, and Aktas B 2007 *Phys. Rev. B* **75** 172405
[31] Huang C, Du Y, Wu H, Xiang H, Deng K, and Kan E 2018 *Phys. Rev. Lett.* **120** 147601
[32] Pan J, Yu J, Zhang Y F, Du S, Janotti A, Liu C X, and Yan Q 2020 *Npj Comput. Mater.* **6** 152
[33] Zhu W, Xie S, Lin H, Zhang G, Wu H, Hu T, Wang Z, Zhang X, Xu J, and Wang Y 2022 *Chin. Phys. Lett.* **39** 128501
[34] Wang H, Lei P, Mao X, Kong X, Ye X, Wang P, Wang Y, Qin X, Meijer J, Zeng H, Shi F, and Du J 2022 *Chin. Phys. Lett.* **39** 047601
[35] Huang B, Clark G, Navarro-Moratalla E, Klein D R, Cheng R, Seyler K L, Zhong D, Schmidgall E, McGuire M A, Cobden D H, Wang Y, Xiao D, Jarillo-Herrero P, and Xu X 2017 *Nature* **546** 270
[36] Gong C, Li L, Li Z, Ji H, Stern A, Xia Y, Cao T, Bao W, Wang C, Wang Y, Qiu Z Q, Cava R J, Louie S G, Xia J, and Zhang X 2017 *Nature* **546** 265
[37] Liu Y, Guo S D, Li Y, and Liu C C 2025 *Phys. Rev. Lett.* **134** 116703
[38] Xia X, Huang Y, Peng B, Wang T, Yi R, Zhao Y, Jiang J, Dai F, Fan Y, Li P, Tu Y, Zhang L, Fang H, and Chen L 2023 *Adv. Mater.* **35** 2303072
[39] Yi R, Jiang J, Yang Y, Zhang Y, Gao S, Zhao Y, Hu J, Su X, Xia X, Peng B, Dai F, Li P, Guan Z, Yang H, Zhu F, Cao J, Wang Z, Fang H, Zhang L, and Chen L 2025 *Nat. Commun.* **16** 464
[40] Chen X, Ren J, Zhu Y, Yu Y, Zhang A, Liu P, Li J, Liu Y, Li C, and Liu Q 2024 *Phys. Rev. X* **14** 031038
[41] Chen X, Liu Y, Liu P, Yu Y, Ren J, Li J, Zhang A, and Liu Q 2025 *Nature* **640** 349
[42] Zhang Y Y, Gao W G, Chen S Y, Xiang H J, and Gong X G 2015 *Comput. Mater. Sci.* **98** 51
[43] Storn R and Price K 1997 *J. Global Optim.* **11** 341
[44] Kresse G and Furthmüller J 1996 *Phys. Rev. B* **54** 11169
[45] Blöchl P E 1994 *Phys. Rev. B* **50** 17953
[46] Kresse G and Joubert D 1999 *Phys. Rev. B* **59** 1758
[47] Perdew J P, Burke K, and Ernzerhof M 1996 *Phys. Rev. Lett.* **77** 3865
[48] Monkhorst H J and Pack J D 1976 *Phys. Rev. B* **13** 5188
[49] Togo A and Tanaka I 2015 *Scr. Mater.* **108** 1

[50] Eriksson F, Fransson E, and Erhart P 2019 *Adv. Theor. Simul.* **2** 1800184
[51] Fransson E, Eriksson F, and Erhart P 2020 *Npj Comput. Mater.* **6** 135
[52] Sanville E, Kenny S D, Smith R, and Henkelman G 2007 *J. Comput. Chem.* **28** 899
[53] Tang W, Sanville E, and Henkelman G 2009 *J. Phys: Condens. Matter* **21** 084204
[54] Kan M, Adhikari S, and Sun Q 2014 *Phys. Chem. Chem. Phys.* **61** 4990
[55] Kan M, Zhou J, Sun Q, Kawazoe Y, and Jena P 2013 *J. Phys. Chem. Lett.* **4** 3382
[56] Lan M, Xiang G, Nie Y, Yang D, and Zhang X 2016 *RSC Adv.* **6** 31758
[57] Liu L, Ren X, Xie J, Cheng B, Liu W, An T, Qin H, and Hu J 2019 *Appl. Surf. Sci.* **480** 300
[58] Jain A, Ong S P, Hautier G, Chen W, Richards W D, Dacek S, Cholia S, Gunter D, Skinner D, Ceder G, and Persson K A 2013 *APL Mater.* **1** 011002
[59] Gao G, Ashcroft N W, and Hoffmann R 2013 *J. Am. Chem. Soc.* **135** 11651
[60] Gao Z Y, Xu W, Gao Y, Guzman R, Guo H, Wang X, Zheng Q, Zhu Z, Zhang Y Y, Lin X, Huan Q, Li G, Zhang L, Zhou W, and Gao H 2022 *Adv. Mater.* **34** 2204779
[61] Bahlawane N and Lenoble D 2014 *Chem. Vap. Depos.* **20** 299
[62] He R, Wang D, Luo N, Zeng J, Chen K Q, and Tang L M 2023 *Phys. Rev. Lett* **130** 046401
[63] Xiang H, Lee C, Koo H J, Gong X, and Whangbo M H 2012 *Dalton Trans.* **42** 823